Journal Pre-proof


# Analysis of contact conditions and its influence on strain rate and temperature in Friction Stir Welding

D.G. Andrade , C. Leitão , N. Dialami , M. Chiumenti , D.M. Rodrigues

PII: S0020-7403(20)33032-0
DOI: https://doi.org/10.1016/j.ijmecsci.2020.106095
Reference: MS 106095

To appear in: *International Journal of Mechanical Sciences*

Received date: 9 July 2020
Revised date: 31 August 2020
Accepted date: 11 September 2020

Please cite this article as: D.G. Andrade , C. Leitão , N. Dialami , M. Chiumenti , D.M. Rodrigues , Analysis of contact conditions and its influence on strain rate and temperature in Friction Stir Welding, *International Journal of Mechanical Sciences* (2020), doi: https://doi.org/10.1016/j.ijmecsci.2020.106095

Highlights

- Evolution of the contact conditions with welding parameters.
- Analysis of strain rate sensitivity to process parameters.
- Prediction of grain size evolution with process parameters.
- Influence of contact conditions on heat generation.
- Analysis of the mechanisms governing material flow.

# Analysis of contact conditions and its influence on strain rate and temperature in Friction Stir Welding

**D. G. Andrade[1,2], C. Leitão[2*], N. Dialami[3], M. Chiumenti[3], D.M. Rodrigues[1]**

[1]ISISE, Mechanical Engineering Department, University of Coimbra, Portugal

[2]CEMMPRE, Mechanical Engineering Department, University of Coimbra, Portugal

[3]Universitat Politècnica de Catalunya, Jordi Girona 1-3, Edifici C1, 08034 Barcelona, Spain, & Centre Internacional de Mètodes Numèrics en Enginyeria (CIMNE), Building C1, Campus Nord UPC, Gran CapitánS/N, 08034 Barcelona, Spain.

*e-mail: carlos.leitao@dem.uc.pt, tel. +(351) 239 790 700, fax: +(351) 239 790 700

## Abstract

In friction stir welding (FSW), the real contact conditions between the tool and the workpiece and the range of strain rates experienced remain quite unclear. In this work, a coupled 3D thermo-mechanical numerical model was used to simulate the FSW process. A Parametric finite element analysis of the evolution of the contact conditions, strain rates and temperatures with the processing parameters, tool dimensions and base material plastic properties was conducted. The numerical model was able to capture the evolution of the mixed slipping/sticking contact conditions with the welding time and welding parameters. The temperature and strain rate gradients obtained in the numerical simulations were validated with experimental data, by calculating the grain size distribution, in the stirred volume, using the Zener-Hollomon parameter. Full sticking, full slipping and mixed slipping-sticking contact domains were identified in a process parameters chart. It was found that, meanwhile the temperature and the sticking fraction evolve in the same way with the processing parameters, the strain rate is mainly determined by the tool rotation speed, varying from an average of 68 to 324 $s^{-1}$, when the tool rotation speed is increased from 300 to 1200 rpm. The contact conditions and the base material plastic properties were also found to mutually influence the material flow. In full sticking contact, high strength materials, with high strain rate sensitivity, may display a similar flow pattern to that of low strength materials. However, coarser and more uniform grain structures may result from the welding of high strength materials, as a result of the narrower range of strain rates experienced during welding combined with high heat input.

**Keywords:** FSW; Contact conditions; Strain rate; Numerical simulation.

## 1. Introduction

During Friction Stir Welding (FSW), the tool rotation and translation movements promote not only the heating by friction of the materials to be joined, but also its plastic deformation under complex loading conditions and variable strain rates. The complex loading conditions, at high temperatures, are responsible for the material flow and for the microstructural phenomena taking place during welding. So the understanding of the mechanisms that govern the plastic deformation during welding, which are conditioned by the contact conditions at the tool/workpiece interface, temperature and strain rates inside the stirred volume, are very important to predict the final microstructure of the welded materials as well as the possibility of defect formation.

Several works attempted to analyse and measure the plastic deformation and the strain rates during FSW, by using different techniques, such as microstructural analysis, tracing materials, analytical models and numerical simulation. Table 1 summarises the strain rate values reported in the literature, determined using the above described techniques, for different base materials and process conditions. Frigaard et al., 2001 [1], Gerlich et al., 2006 [2] and Gerlich et al., 2007 [3] measured the grain size in the stirring zone to compute the strain rate values by using the Zener–Hollomon parameter, in FSW and Friction Stir Spot Welding (FSSW) of Aluminium alloys. Frigaard et al., 2001 [1] calculated strain rate values, between 1 to 20 $s^{-1}$ in FSW of AA6082 and AA7018. According to the authors, these results indicated the occurrence of slipping contact conditions between the tool and the workpiece, since the calculated strain rate values were very low when compared to the angular velocity of the tool. On the other hand, Gerlich et al., 2006 [2] and Gerlich et al., 2007 [3] in FSSW of AA7075 and AA2024, respectively, reported a decrease in the strain rates, from 650 to $20s^{-1}$ and 1600 to $0.6s^{-1}$, by increasing the rotation speed from 1000 to 3000 rpm and 750 to 3000

rpm, respectively. They attributed these results to the local melting of second phase particles. Masaki et al., 2008 [4] determined the strain rate values during FSW of AA1050, by comparing the grain size in the welded zone, with the grain size of specimens loaded in plane-strain compression, under various temperatures and strain rates. Using this technique, the authors found that by increasing the rotation speed from 600 to 1200 rpm the strain rates varied between 1.7 to 2.7 $s^{-1}$.

Chen and Cui, 2009 [5] and Liu et al., 2019 [6] determined the strain rates in FSW of A356 alloy and C1100P copper, respectively, by measuring the distortion of tracer materials in the post-weld microstructure. Chen and Cui, 2009 [5] calculated strain rates between 3.5 to 85 $s^{-1}$ in the leading side of the tool, while Liu et al., 2019 [6] calculated an average strain rate of 20.8 $s^{-1}$ in the band formation zone. The use of tracers has also been used to determine the strain rates and the material flow velocity during FSW by Morisada et al., 2015 [7], Morisada et al., 2015 [8] and Kumar et al., 2018 [9]. Morisada et al., 2015 [7] calculated a maximum strain rate value of almost 15 $s^{-1}$, for the FSW of A1050 at 1000 rpm. Also, in the FSW of A1050 Morisada et al., 2015 [8], observed that the tracing particles rotated around the tool several times, when the rotation speed was higher than 400 rpm, although the angular velocity of the tracer was always lower than the angular velocity of the tool. For rotation speeds lower than 300 rpm the tracing particles stopped rotating around the tool and defects were observed in the weld. Kumar et al., 2018 [9] analysed the influence of the rotation and traverse speeds on the strain rate, in the FSW of a viscoplastic fluid. According to the authors, the tracing particles also rotated several times around the tool pin, up to a maximum velocity of 60 % of the pin angular speed. The tool rotational speed was found to be the main factor governing the strain rates. Increasing the rotation speed from 75 to 425 rpm lead to an increase in the strain rates between 8 and 44 $s^{-1}$.

Chang et al., 2004 [10] and Long et al., 2007 [11] proposed analytical models to estimate the strain rates during welding. Chang et al., 2004 [10] proposed that the strain rates are proportional to the size of the dynamically recrystallised zone and to a fraction of the tool rotational speed, due to the sticking/slipping contact condition at the tool/workpiece interface. Using the previous model, Chang et al., 2004 [10] calculated an increase in the strain rates between 5 to 50 $s^{-1}$ by increasing the rotation speed from 180 to 1800 rpm. The Long et al., 2007 [11] model estimated the strain rates by considering the distance that the tool advance in one rotation, as the initial length of the undeformed material. Then, during the tool rotation, this portion of material is stretched in the front side of the pin and is finally compressed in the trailing side of the pin, where it is deposited. Considering the previous model, Long et al., 2007 [11] calculated an increase in the average strain rates from 20 to 350 $s^{-1}$ by increasing the rotation speed from 544 to 844 rpm, respectively.

Due to the difficulty in calculating the strain rates experimentally during welding, numerical simulation has been used as a tool to determine the strain rates experienced during FSW. Nandan et al., 2006 [12], Nandan et al., 2006 [13] and Nandan et al., 2007 [14] used a three-dimensional viscoplastic model to simulate the FSW of 304 stainless steel, AA6061 aluminium and AISI 1018 steel, respectively. The authors determined maximum strain rate values of 130 $s^{-1}$, 150 $s^{-1}$ and 40 $s^{-1}$, for rotation speeds equal to 344, 300 and 450 rpm, respectively. Du et al., 2020 [15] used numerical simulation to model the FSW of AA2017, AA5083 and AA6082 aluminium alloys and computed strain rate values between 23.16 to 434.25 $s^{-1}$ by varying the rotation speed from 100 to 1100 rpm. Mukherjee and Ghosh, 2010 [16] used two-dimensional finite-element simulation using ABAQUS, to model the FSW of AA5083 aluminium alloy. The authors concluded that a 0.1 ratio between the base material velocity matrix and the

tool velocity, best characterised the material flow. For these conditions, a maximum strain rate of 87 $s^{-1}$ was determined. Ammouri et al., 2015 [17] used a 3D thermo-mechanically coupled FE model to simulate the FSW of AZ31B, under different rotation and traverse speeds. The authors observed that the strain rates increased with the rotation and traverse speeds. Although, the rotation speed presented higher influence on the strain rate values than the traverse speed. Sharghi and Farzadi, 2018 [18] used a three-dimensional model based on the computational fluid dynamics to simulate dissimilar welding of AA6061/Al-$Mg_2Si$ aluminium alloys. The authors computed a maximum strain rate of 975 $s^{-1}$ near the top surface of the workpiece at the outer edge of the tool shoulder.

The contact conditions at the tool/workpiece interface are also critical to understand the welding mechanisms occurring during FSW, although they are difficult to study experimentally. In general, the contact conditions are considered to be fully sticking [19–27] or fully slipping [19,24,28–30]. However, this assumption may be restrictive in order to simulate the welding process accurately. Some works have also considered the partial slipping/sticking phenomena during the welding process by prescribing imposed velocity profiles at the tool/workpiece interface [19,24,31–33].

Considering all the works analysed, it is possible to conclude that the calculated strain rate values widely vary, in accordance with the different measurement techniques, process parameters, contact conditions and base materials used. In current work, a coupled three-dimensional thermo-mechanical model was used to simulate the evolution of the mixed slipping/sticking contact conditions and to compute the strain rates and temperatures during FSW of different base materials under a wide range of parametrically varied welding conditions. The range of temperatures and strain rate obtained in the numerical simulations were validated with experimental results and

extrapolated to predict the evolution of the weld microstructure for the different welding conditions tested.

**Table 1 –** Range of strain rates reported in the literature.

| Technique | Author | Base Material | Rotation speed [rpm] | Traverse speed [mm/min] | Strain rate [$s^{-1}$] |
|---|---|---|---|---|---|
| **Microstructural** | Frigaard et al., 2001 [1] | AA6082 and AA7018 | 1500 | 720 | 1 - 20 |
| | Gerlich et al., 2006 [2] | AA7075-T6 | 1000 - 3000 | 0 | 20 - 650 |
| | Gerlich et al., 2007 [3] | AA2024 T351 | 750 - 3000 | 0 | 0.6 - 1600 |
| | Masaki et al., 2008 [4] | AA1050 | 600 - 1200 | 100 | 1.7 - 2.7 |
| **Tracers** | Chen and Cui, 2009 [5] | A356 (Al-7Si-0.3Mg) | 740 | 168 | 3.5 - 85 |
| | Morisada et al., 2015 [7] | A1050 | 1000 | 400 | 13.4 - 15 |
| | Kumar et al., 2018 [9] | Visco-plastic fluid | 75 - 425 | 50-110 | 8 - 44 |
| | Liu et al., 2019 [6] | Copper C1100P | 800 | 150 | 20.8 |
| **Analytical model** | Chang et al., 2004 [10] | AZ31 | 180 - 1800 | 90 | 5 - 50 |
| | Long et al., 2007 [11] | 5083-O, 2219-T87 and 7050-T751 | 544 - 844 | 76.2 | 20 - 350 |
| **Numerical** | Nandan et al., 2006 [12] | 304 Stainless Steel | 300 | 101 | 130 |
| | Nandan et al., 2006 [13] | AA6061 | 344 | 95 | 150 |
| | Nandan et al., 2007 [14] | AISI 1018 | 450 | 25.2 | 40 |
| | Mukherjee and Ghosh, 2010 [16] | AA5083 | 1500 | 50.8 | 87 |
| | Ammouri et al., 2015 [17] | AZ31B alloy | 600 - 2000 | 75 - 900 | 34.8 - 122.5 |
| | Sharghi and Farzadi, 2018 [18] | AA6061/ Al-Mg2Si | 1120 | 120 | 975 |
| | Du et al., 2020 [15] | AA2219, AA5083 and AA6082 | 150-1302 | 100-1100 | 23.16-434.25 |

## 2. Numerical simulation

### 2.1 The finite element model

The contact conditions and the plastic deformation during FSW were studied by using the three-dimensional numerical model proposed by Chiumenti et al., 2013 [34] and

Dialami et al., 2013 [35]. As shown in Figure 1, the finite element model combines three different kinematic frameworks. The tool is modelled in a Lagrangian framework, while the stirring zone and the base material are modelled using Arbitrary Lagrangian/Eulerian (ALE) and Eulerian frameworks, respectively. In order to reduce the computational time, the two-stage solution strategy proposed by Dialami et al., 2017 [36] was used. The coupled thermo-mechanical problem is solved by using the thermal and mechanical sub-problems, shown in Table 2, sequentially for each time step. The nomenclature of the variables used is shown in Table 3. In the numerical model it was assumed that 90% of the plastic dissipation was converted into heat. For a more detailed explanation of the thermal and mechanical models, and of the computational framework, see Refs. [35–39].

**Table 2** – Formulation.

| **Mechanical partition** | |
|---|---|
| $\nabla \cdot s + \nabla p + \rho_o b = 0$ | Momentum balance equation |
| $\nabla \cdot v = 0$ | Continuity equation |
| $\dot{\varepsilon} = \nabla^s v$ | Kinematic equation |
| $\sigma_{eq} = \sqrt{3/2}\,(s:s)^{1/2}$ | Equivalent stress |
| $\dot{\varepsilon}_{eq} = \sqrt{2/3}\,(\dot{\varepsilon}:\dot{\varepsilon})^{1/2}$ | Equivalent strain rate |
| **Thermal partition** | |
| $\rho_0 c\left(\frac{1}{\xi}\frac{dT}{dt} + (v - v_{mesh}) \cdot \nabla T\right) - \nabla \cdot (k\,\nabla T) = D_{mesh}$ | Energy balance equation |
| $D_{mesh} = \theta s:\dot{\varepsilon}$ | Viscoplastic dissipation |
| $q_{conv} = h(T - T_{env})$ | Heat convection |
| $q_{cond} = h_{cond}(T - T_{tool})$ | Heat conduction |

**Table 3** – Nomenclature.

| | |
|---|---|
| $s$ | Stress deviator |
| $p$ | Pressure |
| $\rho_0$ | Density in the reference configuration |
| $b$ | Body forces vector per unit of mass |
| $v$ | Velocity field |
| $\dot{\varepsilon}$ | Strain rate |
| $c$ | Specific heat |
| $T$ | Temperature |

| | |
|---|---|
| $v_{mesh}$ | Velocity of the mesh |
| $k$ | Thermal conductivity |
| $\theta$ | Fraction of plastic dissipation |
| $h_{conv}$ | Heat transfer coefficient by convection |
| $h_{cond}$ | Heat transfer coefficient by conduction |
| $\xi$ | Speed-up factor |
| $T_{env}$ | Environmental temperature |
| $T_{tool}$ | Tool temperature |

In this work, a square shaped workpiece with 160×160 mm was used to simulate the base material. The tool was simulated with a flat shoulder with a concentric cylindrical pin. A mesh with 32000 nodes and 180000 tetrahedral elements was used in the numerical simulations. In order to understand the influence of the process parameters on the contact conditions and on the plastic deformation during welding, in the numerical simulations, the rotation ($\omega$) and traverse ($v$) speeds were varied between 300 to 1200 rpm and 250 to 1000 mm/min, respectively. The tool pin diameter ($D_p$), pin length ($p_l$), shoulder diameter ($D_s$) and base material thickness ($t$) were varied in the range of 4 to 10 mm, 1.8 to 8.5 mm, 12 to 30 mm and 2 to 10 mm, respectively. According to Andrade et al., 2020 [40], this range of welding velocities, tool dimensions and plate thicknesses represent the majority of the welding conditions tested in the FSW works on aluminium alloys. As in Andrade et al., 2020 [40], in current work, the influence of the tool dimensions on the welding outputs was considered by using the geometry parameter ($G$), that corresponds to the contact area between the tool and the workpiece,

$$G = \frac{\pi}{4} D_p^2 + \pi D_p p_l + \frac{\pi}{4}\left(D_s - D_p\right)^2. \quad (1)$$

The combination of base material thicknesses, pin and shoulder diameters and respective geometry parameters used in current numerical simulations are summarised in Table 4. These combinations were set according to Zhang et al., 2012 [41] and Prado et al., 2001 [42], who recommended a shoulder diameter to plate thickness relation

equal to $D_s = 2.2t+7.3$ and a shoulder to pin diameter ratio equal to $D_s/D_p=3$, respectively. Also, a pin length to plate thickness ratio equal to 0.85 was considered.

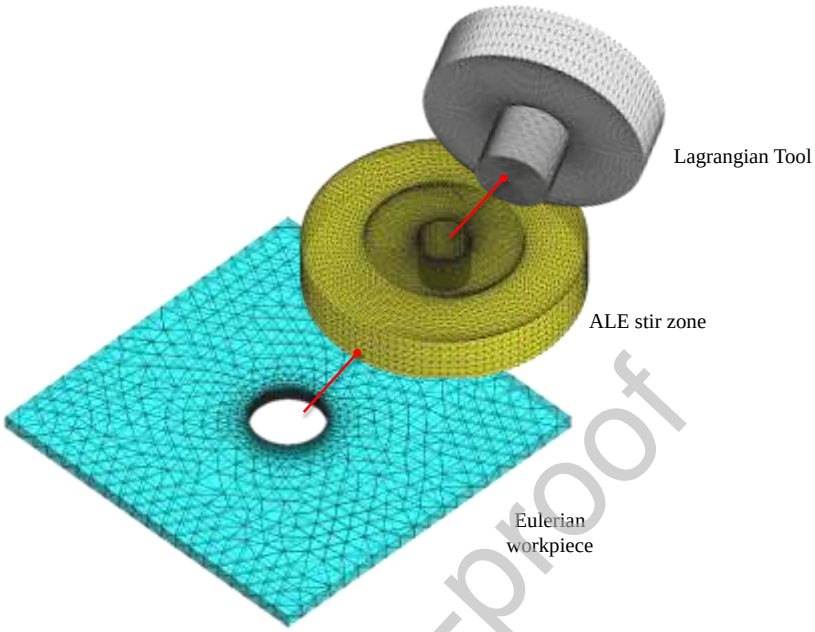


**Figure 1 –** Numerical model and respective subdomains: Lagrangian, ALE and Eulerian zones.

**Table 4 –** Base material thicknesses, shoulder diameters, pin diameters and geometry parameters used in the numerical simulations.

| $t$ [mm] | $D_s$ [mm] | $D_p$ [mm] | $G$ [mm$^2$] |
|---|---|---|---|
| 2 | 12 | 4 | 134 |
| 6 | 18 | 6 | 351 |
| 10 | 30 | 10 | 974 |

## 2.2 The base materials modelled

The base material plastic behaviour was modelled by using the Norton-Hoff constitutive model,

$$\sigma_{eq}\left(\dot{\varepsilon}_{eq}, T\right) = \sqrt{3}\mu\left(\sqrt{3}\dot{\varepsilon}_{eq}\right)^{m}, \quad (2)$$

where $\sigma_{eq}$ is the equivalent stress, $\dot{\varepsilon}_{eq}$ is the equivalent strain rate and $\mu$ and $m$ are constants that determine the strength and the strain rate sensitivity, respectively, of the base material. Some conceptual materials were considered in this analysis. The base

materials stress-strain rate curves, for a constant temperature of 25 ºC and 550 ºC, and the stress-temperature curves, for a constant strain rate of 100 $s^{-1}$, are represented in Figure 2a to 2c. In the figure, the base material represented by the yellow line was modelled using the AA6063-T6 constitutive properties from Dialami et al., 2017 [37]. The constitutive properties of this material, which will be labelled as reference material, were used in most of the analysis that follows. The remaining base materials used in the analysis were conceptually developed by varying $\mu$ and $m$ values, taken from the reference material, from -90 % to +100 % as shown in Figure 2. The *HSHSRS* and the *HSLSRS* are high strength materials ($\mu$ = +100 %) but with high ($m$ = +100 %) and low ($m$ = -90 %) strain rate sensitivity, respectively. On the other hand, the LSHSRS and LSLSRS are low strength materials ($\mu$ = -90 %), but with high ($m$ = +100 %) and low ($m$ = -90 %) strain rate sensitivity, respectively. The conceptual materials were exclusively used in a parametric analysis on the influence of the plastic properties of the base materials on the material flow and temperature and strain rate distributions during welding.

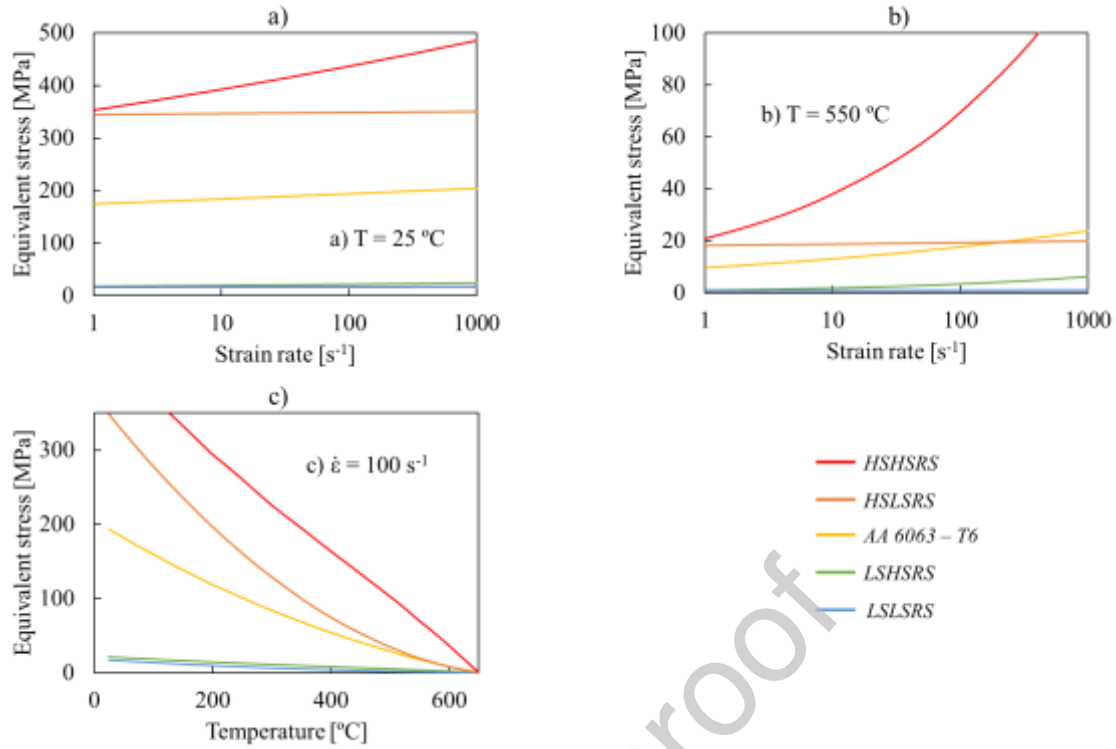


**Figure 2 –** Stress-strain rate curves at a constant temperature of 25 ºC (a) and 550 ºC (b), and stress-temperature curves at a constant strain rate of 100 $s^{-1}$ (c). Labels *HSHSRS* and *HSLSRS* denote high strength materials with high and low strain rate sensitivity, respectively. Labels *LSHSRS* and *LSLSRS* denote low strength materials with high and low strain rate sensitivity, respectively.

### 2.3 The friction law and the contact conditions

The Norton's friction law was used to model the friction between the tool and the workpiece:

$$\tau = a(T)\|\Delta v_s\|^{q-1}\Delta v_s. \quad (3)$$

In the equation, $\tau$ is the friction shear stress, $\Delta v_s$ is the relative sliding velocity between the tool and the workpiece, $q$ is the sensitivity to the sliding velocity and $a(T)$ is the consistency parameter given by

$$a(T) = -\alpha_f K(T), \quad (4)$$

where $\alpha_f$ is the friction coefficient and $K(T)$ is the temperature dependent material consistency. Considering an almost uniform temperature distribution at the contact interface, $a(T)$ may be assumed constant. In order to ensure that the mixed contact conditions characteristic of the FSW process were accurately captured by the numerical

model, $a(T)$ values ranging from 50 to 500 MPa, were tested. With this selection, several friction coefficients were assumed, since $K(T)$ is a material related constant. The sensitivity to the sliding velocity parameter was assumed to be constant ($q$ = 0.5) [37].

The contact conditions between the tool and the workpiece were assessed by measuring the sticking fraction (δ), as suggested by Schmidt et al., 2003 [43]:

$$\delta = \frac{v_{BM}}{v_{tool}} \ . \quad (5)$$

In the equation, $v_{BM}$ represents the velocity of the base material, at the tool/workpiece interface, and $v_{tool}$ is the tool velocity. According to Schmidt et al., 2003 [43], when the sticking fraction is equal to one, it means that the contact is 100 % sticking. When the sticking fraction is equal to zero, it means that the contact is 100 % slipping.

## 3. Analysis of results

### 3.1. Sensitivity analysis on contact conditions

To determine whether the mixed slipping/sticking contact conditions occurring in the FSW process were accurately captured by the numerical model, $a(T)$ values ranging from 50 to 500 MPa were tested using the AA 6063 alloy constitutive properties for modelling the base material, a tool with geometry parameter $G$ = 351 mm$^2$ and rotation and traverse speeds of 600 rpm and 250 mm/min, respectively.

Figures 3a and 3b compare the evolution of the base material and tool velocities, at the tool/workpiece interface, in two different stages of the FSW process, i.e. at the beginning of the welding process ($t$ = 0.04s) and after steady state conditions are reached ($t$ = 5s). The figure refers to numerical simulations performed using $a(T)$ equal

to 90 and 500 MPa. In Figures 3c and 3d is compared the distribution of the sticking fraction, calculated using the velocity profiles of Figures 3a and b, respectively. In the next, to characterise the contact conditions, the average sticking fraction ($\delta_{avg}$), which is the average of the sticking fraction values calculated for all the points along the tool/workpiece interface, will be used.

Analysing Figure 3 it is possible to conclude that, in both numerical simulations, the tool and the material velocities increase with the radial distance from the tool axis, and its maximum values are reached at the outer shoulder edge. The figure also enables to conclude that, irrespective of $a(T)$, the sticking fraction increased with the welding time, satisfactorily reproducing the evolution of the contact conditions during the dwelling period at the beginning of the FSW process. Although, meanwhile for the simulations performed with $a(T)$ = 90 MPa, slipping contact conditions ($\delta_{avg} \approx 0$) prevailed at the initial stage of the welding process ($t$ = 0.04s), for the simulations performed with $a(T)$ = 500 MPa, a large sticking fraction ($\delta_{avg} \approx 0.8$) was registered since the beginning of the welding process. When using $a(T)$ =90 MPa, once steady state conditions were reached ($t$ = 5s), mixed slipping/sticking contact conditions ($\delta_{avg} \approx 0.7$) were developed. On the other hand, when using $a(T)$ = 500 MPa, full sticking ($\delta_{avg} \approx 1$) prevailed after steady state conditions were reached. Another important difference between the simulations performed with the different consistency parameter values is that, for the simulations ran with $a(T)$ = 90 MPa, the contact conditions were not symmetrical nor uniform along the tool diameter, since the beginning of the welding process, being registered higher sticking fractions at the retreating side (*RS*) than at the advancing side (*AS*) of the tool. However, for the simulations ran with $a(T)$ = 500 MPa, contact conditions were almost symmetrical and became uniform, at the shoulder/workpiece interface, when steady state conditions were reached. For $a(T)$ = 90

MPa, the sticking fraction was also higher, at the inner shoulder diameter, where the tool velocity is lower and the weld nugget is formed due to the dragging of the material from the shoulder influence zone to the pin influence zone [44].

The analysis performed in the previous paragraph showed important differences in contact conditions at the tool/workpiece interface when different values were assumed for the consistency parameter in the Norton friction law. So, in order to better understand the evolution of the contact conditions with $a(T)$, and its influence on heat generation and material flow, numerical simulations were ran using a varied range of tool rotational speeds (300, 600, 900 and 1200 rpm), which is the main factor governing the heat generation in FSW [40]. Figures 4a and 4b show the evolution of the average sticking fraction with $a(T)$ and with the rotation speed, respectively. In the figures, it is also plotted the evolution of the welding temperature for the range of welding conditions tested. The welding temperature was calculated by computing the average temperature in the stirring volume, i.e. considering only the amount of material with equivalent strain rate values higher than zero.

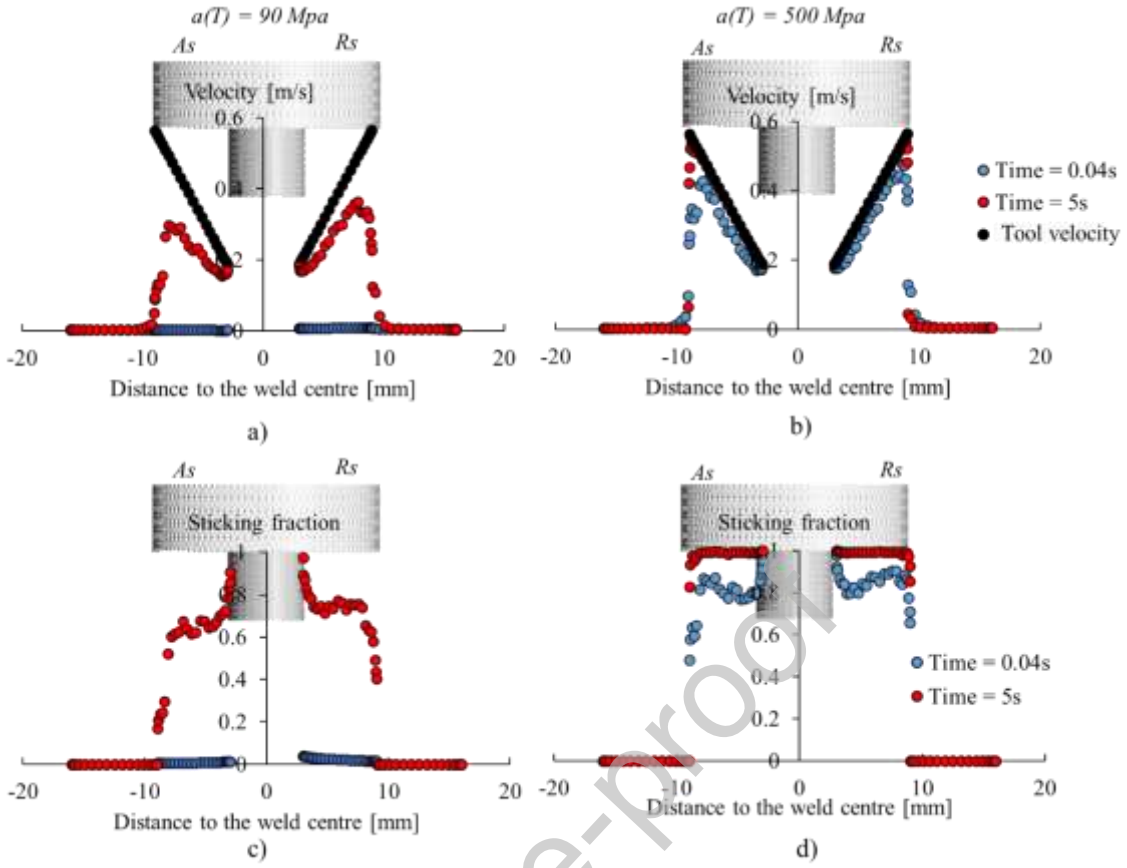


**Figure 3 –** Evolution of the base material velocity at the tool/workpiece interface (a and b) and of the sticking fraction (c and d) with the welding time. Labels $a(T)$, *As*, *Rs* denote consistency parameter, advancing side and retreating side, respectively.

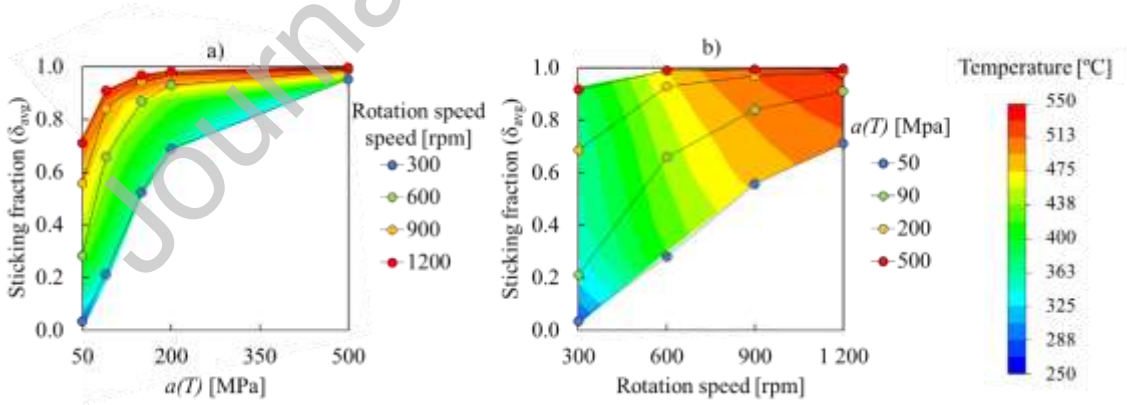


**Figure 4 –** Evolution of the average sticking fraction with $a(T)$ (a) and rotation speed (b). Label $a(T)$, denote consistency parameter.

Analysing Figure 4a, it can be concluded that, independently of the rotation speed, the sticking fraction increases with $a(T)$. For $a(T)$ < 200 MPa, slipping contact

and mixed slipping/sticking contact prevail, depending on the tool rotational speed. For $a(T)$ > 200 MPa, sticking contact prevails, mainly for rotation speeds higher than 600 rpm. Figure 4 also shows that the low temperatures associated with the very low rotation speed of 300 rpm [40], is only simulated for $a(T)$ < 100 MPa and that the transition between prevalent slipping, at low rotation speeds, to prevalent sticking, at high rotation speeds, is only simulated for $a(T)$ = 90 MPa. Based on these results, $a(T)$ = 90 MPa was selected to be used in the analysis of the evolution of the contact conditions and strain rate with process parameters. In the next, this option will be validated based on literature and experimental results.

### 3.2.Validation of the model

A relationship between the process parameters and the welding temperatures was already established and validated by Andrade et al., 2020 [40]:

$$\begin{cases} T = K_T C_T^{\varphi} \text{ for } C_T < 20000 \\ T = 590ºC \text{ for } C_T \geq 20000 \end{cases} \quad (6)$$

In these relationships, $C_T$ is the temperature coefficient and $K_T$ and $\varphi$ are constants related to the base material properties. For aluminium alloys, the authors determined that for $K_T$ and $\varphi$ equal to 50 and 0.25, respectively, a good fitting for a large number of literature results was obtained. The temperature coefficient is given by

$$C_T = \frac{G\omega}{\sqrt{vt}}. \quad (7)$$

In Figure 5 the temperature values previewed by the analytical model (Eq. 6) are compared with the numerical results obtained in the numerical simulations, using $a(T)$

= 90 MPa and considering the constitutive properties of the AA6063 alloy and all welding conditions tested in this work. In the figure is plotted a rectangle in blue, highlighting the evolution of temperature for predominant sliding conditions ($\delta_{avg} \leq 0.2$) and a rectangle in grey highlighting the evolution of temperature results for the simulations in which $\delta_{avg} > 0.2$. The correlation between the analytical model and the results of the numerical simulations was assessed by the percentage error between the average of the temperatures obtained from the numerical simulations and the average of the temperatures previewed by the model. Analysing the figure, it is possible to conclude that for sticking fraction values lower than 0.2, the percentage error between the analytical and the numerical simulation results is 25 %. For these welding conditions, the temperatures were always inferior to the ones predicted by the analytical model. For sticking fraction values higher than 0.2, the percentage error is inferior to 3 %, showing a very good agreement between the numerical results with the ones predicted by the analytical model. These results indicate that, in the domain of mixed contact conditions and full sticking, the welding temperatures are determined by the process parameters and tool dimensions, but the same is not true when sliding contact prevails, i.e. in a temperature interval conducting to the production of defective welds due to the very low heat input [8,45]. This may be explained assuming that in the full sliding domain an accurate knowledge of the friction coefficient ($\alpha_f$) is required in order to accurately model the FSW process. However, the figure also shows that for mixed sliding/sticking conditions, the temperature may be accurately previewed using $a(T)$ = 90 MPa for modelling the contact conditions.

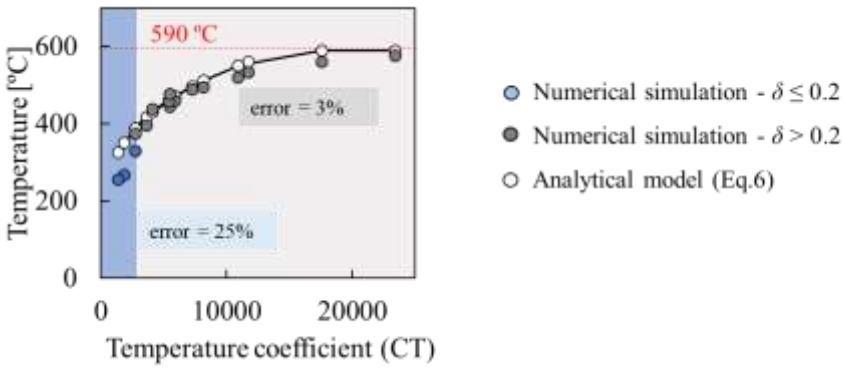


**Figure 5 –** Comparison between the temperature values previewed by the analytical model (Eq. 6) with the temperatures computed by the numerical results, for $\delta_{avg} \leq 0.2$ (a) and $\delta_{avg} > 0.2$ (b). ). Label $\delta_{avg}$, denote average sticking fraction.

In Figure 6 is now shown a cross-section of a weld performed in the AA6082-T6 aluminium alloy using a tool with a geometry parameter of 475 $mm^2$ and rotation and traverse speeds of 500 rpm and 200 mm/min, respectively. In figure are displayed the streamlines representing the material flow around the tool, determined as in Dialami et al., 2014 [46] . The figure also shows the strain rate and temperature distributions, in the weld cross section, obtained when simulating the experimental FSW test. Despite the room temperature properties of the AA6063-T6, to which refer the material constitutive properties used in the numerical simulations, and the AA6082-T6 alloys, used to fabricate the weld in the figure, are different, at the very high temperatures reached during FSW, it is expected that both alloys display similar properties and that the numerical and experimental results may be compared. Actually, analysing the streamlines in Figure 6 it is possible to conclude that, for the FSW conditions modelled, the numerical simulations preview that the material is stirred under the shoulder for more than one revolution. This prevision is corroborated by the cross-section of the weld, which displays a large shoulder influence zone. However, in order to better demonstrate the good agreement between the numerical and the experimental results, the grain size (GS) distribution in weld nugget, represented in Figure 7, was compared

with the grain size distribution calculated using the temperature and strain rate distributions displayed in Figure 6.

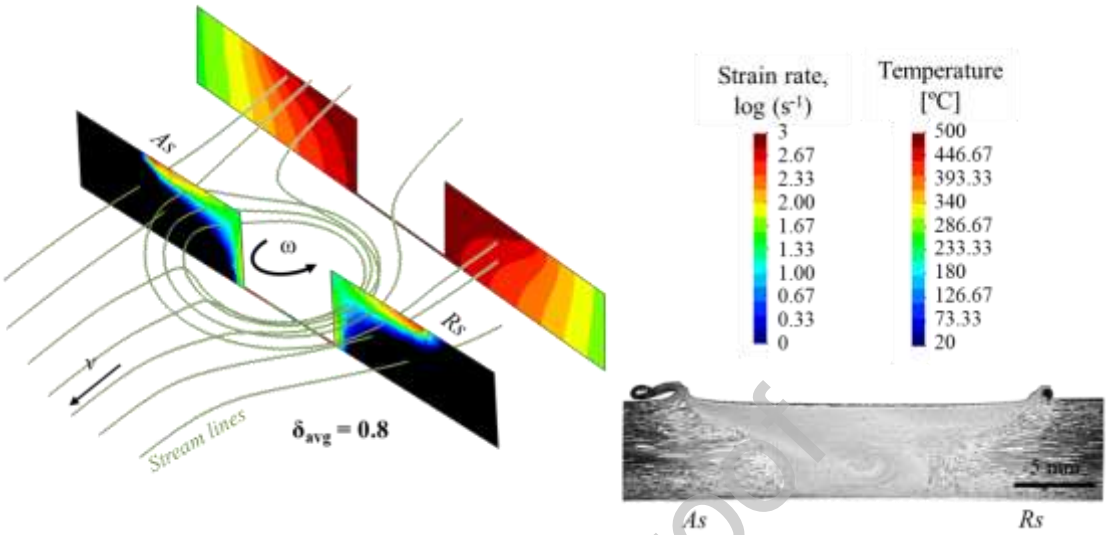


**Figure 6 –** Comparison between the AA6082-T6 weld cross section, with the streamlines, temperature and strain rate fields obtained through numerical simulation. Labels *As*, *Rs*, *δ*, *ω* and *v* denote advancing side, retreating side, sticking fraction, rotation speed and traverse speed, respectively.

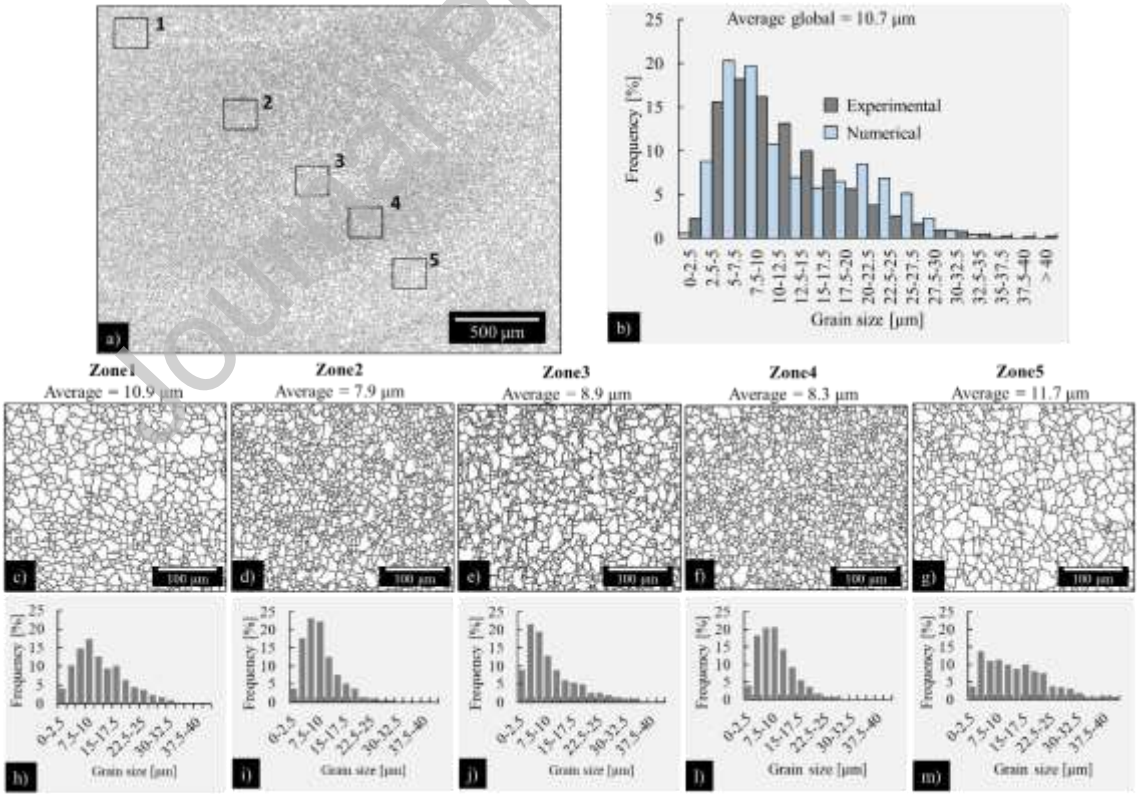


**Figure 7 –** Microstructure and grain size distribution in the weld nugget.

Figure 7a and 7b clearly illustrate the large dispersion in GS inside the nugget of the weld in Figure 6. According to Leal et al., 2008, [44] the onion rings are composed by intercalated layers, which result from the incorporation of the plasticised material dragged under the shoulder into to the shear layer around the pin. Magnifications of the microstructure in different locations of the nugget, identified by numbers 1 to 5 in Figure 7a, as well as the grain size distribution in these different regions, are shown in Figures 7c to 7m. Analysing the figure, it is possible to observe zones with smaller grain size intercalated with zones with larger grain size. As it is known, in thermo-mechanical processes with severe plastic deformation, such as FSW, the dynamic recrystallisation phenomena contribute to the grain refinement in the weld nugget. According to Huang and Logé, 2016 [47], the recrystallisation kinetics and the recrystallised grain size increases with increasing temperatures and decreasing strain rates. The Zener-Hollomon parameter ($Z$)

$$Z = \dot{\varepsilon}\left(\frac{Q}{RT}\right), \tag{8}$$

have been used to incorporate the strain rates ($\dot{\varepsilon}$) and the deformation temperature ($T$) into a single parameter by several works in FSW [1–3,10,48]. In the equation, $R$ is the gas constant and $Q$ is the deformation activation energy. The relation between the Zener-Hollomon parameter and the recrystallised grain size ($d$) is given by [10,48]

$$ln(d) = a - b \times ln(Z), \tag{9}$$

where $a$ and $b$ are material constants. For the AA 6063 aluminium alloy, the activation energy is about 153 kJ/mol [49]. Fitting the experimental results in Figure 7, it was determined that $a$ and $b$ constants are equal to 15 and 0.44, respectively. In Figure 7b, the grain size distribution obtained from the microstructural analysis is compared with the grain size distribution obtained through the numerical simulation, using Eq. 8 and 9 and the constants determined using the experimental results. Analysing the figure, it is

possible to conclude that the grain size distribution estimated using the numerical results satisfactorily reproduce the experimental ones, which validates the numerical model. The differences between the numerical and experimental results may be explained considering the differences in constitutive properties between the AA6063 and AA6082 alloys, and also, by the fact that no mesh refinement was performed in order to capture more accurately the strain rate and temperature gradients inside the stirred volume.

### 3.3.Influence of process parameters on the thermomechanical conditions

The influence of the process parameters on the contact conditions and strain rates developed during FSW was analysed by performing numerical simulations, using the constitutive properties of the AA6063-T6 alloy, the reference material in this study, $a(T)$ = 90 MPa and varying the tool traverse and rotation speeds, as well as the tool dimensions, represented by the geometry parameter.

In a previous investigation, from the current authors [40], it was already demonstrated that the rotation speed and the tool dimensions were the main factors governing the heat generation in FSW. This conclusion is also illustrated in Figure 8 of this manuscript, which shows the evolution of the temperature (coloured maps) as a function of $\omega$ and $G$. However, in addition to the temperature evolution, the figure also shows the evolution of the average sticking fraction (discontinuous lines) and of the average strain rate (continuous lines), in the stirred material volume. Analysing the results, it is possible to conclude that in the lower temperatures domain, the sticking fraction evolves with $G$ and $\omega$ in the same way as the temperature, i.e., the dashed lines almost follow the contour of the isotherms. On the other hand, in the higher temperatures domain, corresponding to large values of $G$ and $\omega$, meanwhile the sticking fraction becomes very high and almost constant, the temperature continues to increase

with $G$ and $\omega$. The graphic also shows that the average strain rate also increases with the rotation speed, being mainly determined by this parameter.

Since both the temperature and the strain rate deeply vary in the full sticking domain ($\delta > 0.9$), it is possible to conclude that the increase in heat generation is due to an increase in the adiabatic heat generation associated with the plastic deformation of the stirred material at very high strain rates [50–52]. Actually, Andrade et al., 2020 [40], showed that the volume of the stirred material deeply increases in this domain of temperature and tool dimensions. In order to illustrate the previous assumptions, in Figure 9 are now shown the streamlines that represent the material flow around the tool during welding, together with the distribution of the logarithmic equivalent strain rate in the weld cross-sections, for some of the welding conditions whose temperatures are represented in Figure 8. Analysing the figure, it is possible to conclude that irrespective of the welding parameters, the computed strain rate values widely vary in the weld cross-section. It is also important to observe that the strain rate values are very high at the outer edge of the tool shoulder, where the tool velocity gradients are higher and a singularity in the strain rate distribution is determined by the numerical model.

Analysing the streamlines for the weld produced with a tool with geometry parameter of 351 $mm^2$ and rotation and traverse speeds of 600 rpm and 250 mm/min, respectively, it is possible to conclude that the material is stirred from the advancing to the retreating side, being deposited approximately one pin diameter backwards, relative to the tool translational movement. Increasing the traverse speed from 250 to 1000 mm/min lead to a slight decrease in the sticking fraction, from 0.7 to 0.5, but the material is still extruded around the tool and deposited at the advancing side, in the rear of the tool. The streamlines are nearest to the tool pin, since the stirred volume decreases when increasing the traverse speed. When the rotation speed is decreased to

300 rpm, the sticking fraction reduces to 0.2 and the material does not complete a full rotation around the tool, which is usually associated to the formation of tunnel defects at the advancing side of the tool [8,45]. On the other hand, when increasing the rotation speed to 1200 rpm, it is possible to observe that the material rotated several times under the shoulder, increasing the strain rate in the stirred volume. A similar material flow pattern was registered when welding with rotation and traverse speeds of 600 rpm and 250 mm/min, respectively, but increasing the tool dimensions from a geometry factor of 351 to 974 $mm^2$. Actually, the figure shows that the material only rotated several times around the tool when the contact conditions were close to full sticking ($\delta_{avg} \geq 0.9$), i.e., in the very high temperatures domain of Figure 8. Another important remark is that the formation of weld defects, due to the absence of proper material stirring, was only previewed when the contact conditions were close to full sliding ($\delta_{avg} = 0.2$).

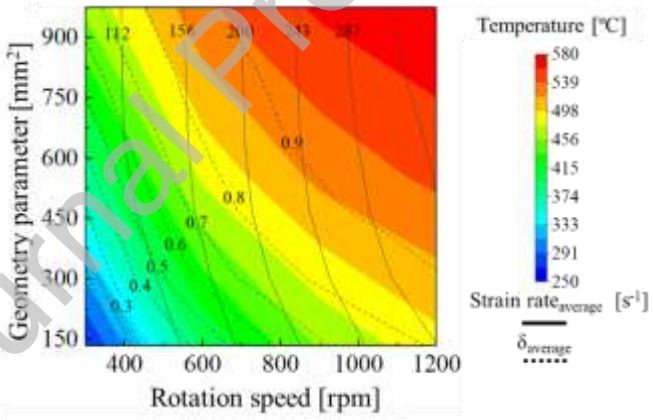


**Figure 8 –** Evolution of the welding temperatures, average strain rate (continuous lines) and average sticking fraction (discontinuous lines) with the rotational speed and geometry parameter.

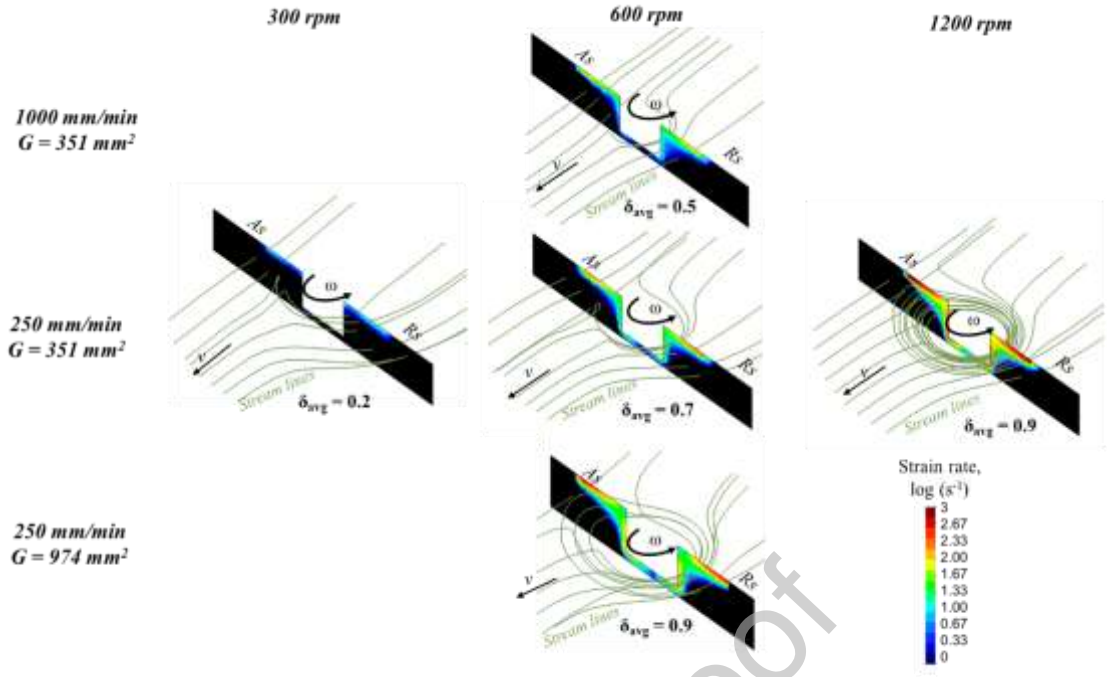


**Figure 9 –** Evolution of the welding streamlines and logarithmic equivalent strain rate maps with the processing parameters. Labels *As*, *Rs*, *δ*, *ω* and *v* denote advancing side, retreating side, sticking fraction, rotation speed and traverse speed, respectively.

In the previous section it was demonstrated that the strain rate and the temperature fields, obtained in the numerical simulation, enabled to preview with reasonable accuracy the grain size distribution in the stirred volume. In this way, in the next, the influence of the process parameters on the thermomechanical conditions in FSW will be analysed by plotting the GS distribution, for different welding conditions, versus the strain rate and temperature. In Figure 10 the evolution of the grain size versus the temperature and strain rate is compared for samples processed with different traverse speeds (Figure 10a), rotation speeds (Figure 10b) and geometry parameters (Figure 10c). In each figure, the largest strain rate values, corresponding to local singularities at the outer tool diameter, were excluded from the graphics, by only considering the values within the strain rate 99th percentile.

Analysing Figure 10a, where it is represented the grain size distribution for the samples welded with two different traverse speeds and two different tools, using 600

rpm rotation speed, it is possible to conclude that meanwhile the range of strain rates was similar in all welding conditions, the temperature ranges were markedly different. For the smaller tool modelled, was registered a much broader welding temperatures range when welding at 250 mm/min (≈ 445 ºC) than when welding at 1000 mm/min (≈ 376 ºC). However, when welding at 1000 mm/min, with a tool with much higher shoulder diameter ($G$ = 974 mm$^2$), the average temperature (≈ 480 ºC) was higher than when welding at 250 mm/min and with the lower shoulder diameter tool (≈ 445 ºC). The similarities in strain rate values between the three welding conditions are associated to the fact of being used the same rotation speed in all cases, i.e. the main parameter governing the strain rate in the stirred volume. So, based on the analysis of the data provided in the graphic, it can be concluded that the important differences in grain size distribution between the welds performed with the different traverse speeds, and the same tool, results from the differences in temperature distribution, in the two samples, associated to the strong influence of the traverse speed on the heat dissipation during welding [40]. The heat dissipative effect of the high traverse speed was suppressed when the heat generation was increased by increasing the shoulder diameter. This conducted to an important rise in the maximum temperature and the production of a coarse grain microstructure is previewed.

Analysing now Figure 10b, where is plotted the prevision for the grain size distribution in the nugget of welds performed with different rotation speeds but a constant traverse speed of 250 mm/min and the same tool ($G$ = 351 mm$^2$), it can be concluded that the coarser grain sizes were previewed for the sample processed with the highest rotation speed. Actually, the figure once again demonstrates that the maximum strain rate deeply increases when increasing the rotation speed. However, since the temperature follows the same trend, and its influence on grain size prevail over that of

the strain rate, the use of high rotation speeds conduct to the production of welds with a large number of coarse grains intercalated with bands of very small grain size. When diminishing the rotation speed, the average grain size diminishes and the grain size distribution becomes narrower.

Finally, Figure 10c refers to welds produced with constant rotation and traverse speeds of 600 rpm and 250 mm/min, respectively, but with tools with different sizes. The figure shows that, since the same rotation speed was used in all tests, the strain rate range was very similar for all the samples. However, due to the strong influence of the tool dimensions on the heat generation, the temperatures were very different, being much higher for the weld produced with the larger tool. For these welding conditions, an almost uniform coarse grain structure is previewed by the numerical simulation. Figure 10c also shows the important influence of the tool dimensions on the microstructure, which is illustrated by the results relative to welds performed with the largest tool geometry and a rotation speed of 300 rpm. For this welding condition, larger grain sizes are previewed than when welding with lower tool dimensions but a higher tool rotational speed of 600 rpm. This result is mainly a consequence of the lower strain rates associated with the rotation speed of 300 rpm, since the temperatures are similar to that of welding operations performed with smaller tools but higher rotation speeds.

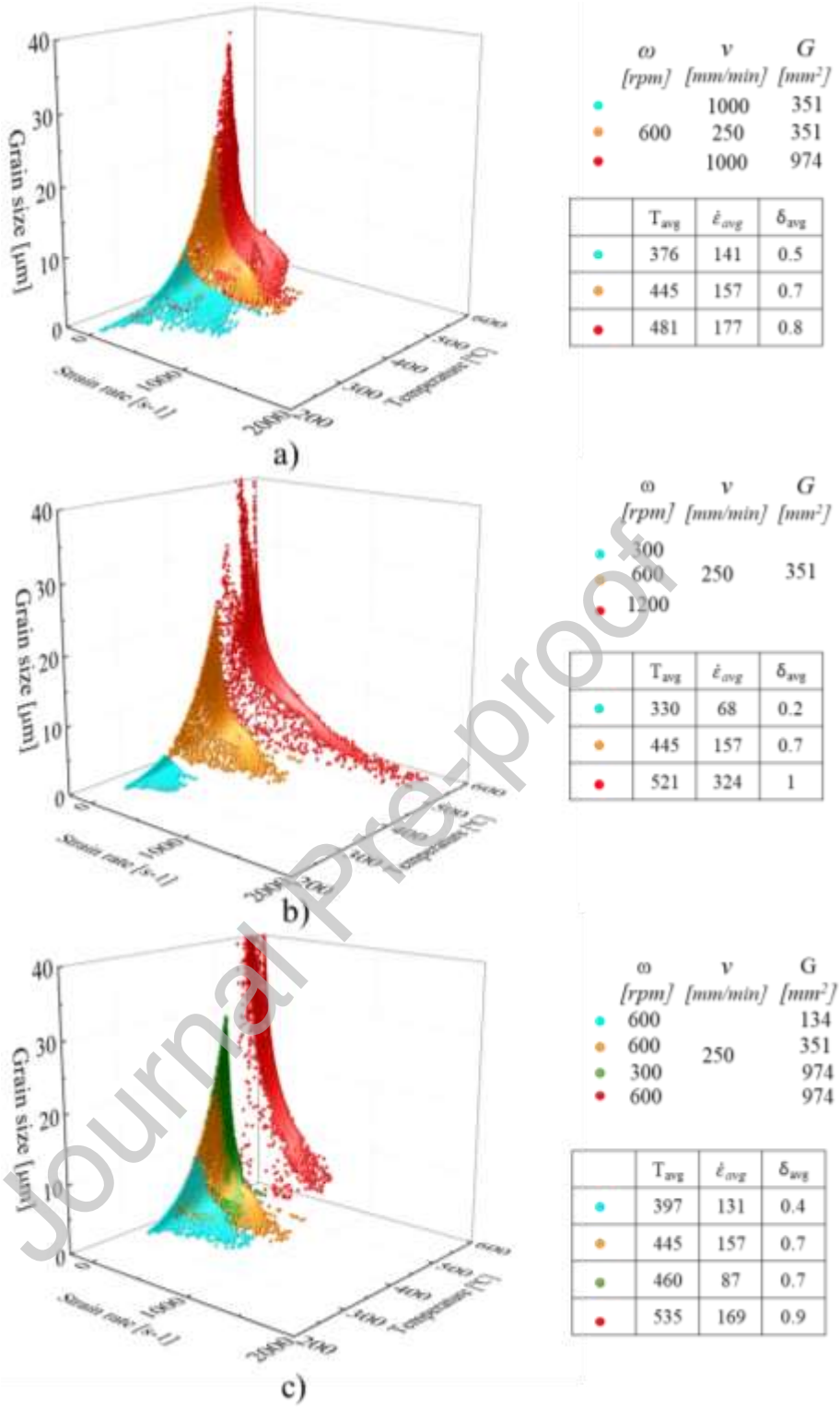


**Figure 10 –** Evolution of the grain size versus the temperature and strain rate for different traverse speeds (a), rotation speeds (b) and geometry parameters (c). Labels $\omega$, $v$ and $G$ denote rotation speed, traverse speed and geometry parameter, respectively. Labels $T_{avg}$, $\dot{\varepsilon}_{avg}$ and $\delta_{avg}$ denote average temperature, strain rate and sticking fraction, respectively.

### 3.4.Influence of base materials plastic properties on the thermomechanical conditions

As previously described, when introducing the base materials modelled, several conceptual materials were generated in order to analyse the influence of the plastic properties of the base materials on the thermomechanical conditions developed during FSW. The base materials plastic behaviour, for temperatures of 25 ºC and 550ºC, and for a constant strain rate of 100 $s^{-1}$, was already represented in Figures 2a to 2c. The figure shows that meanwhile for the low strength conceptual materials the strain rate sensitivity has no important influence on the material strength at very high temperatures, for the high strength conceptual material, the strain rate sensitivity may be responsible for a large difference in strength, at high temperatures, relative to lower strength materials and the high strength material with lower strain rate sensitivity. Actually, Figure 2 shows that the strength of the HSLSRS, at high temperatures and high strain rates, is even lower than that of the reference material, which has much lower strength at room temperature but higher strain rate sensitivity.

In Figure 11 are now compared, for all the base materials modelled, the streamlines that represent the material flow around the tool during welding, as well as the distribution of the logarithmic equivalent strain rate in the weld cross-sections. The results shown in the figure were obtained for constant rotational and traverse speeds of 600 rpm and 250 mm/min, respectively, and a tool with a geometry parameter of 351 $mm^2$. A consistency parameter $a(T)$ = 500 MPa was used in order to ensure full sticking contact for all the materials, enhancing the influence of the plastic properties of the base materials on the material flow and heat generation in FSW. Analysing the figure, it is possible to conclude that, in spite full sticking contact was simulated for all the base materials ($\delta_{avg}$ = 1), the material flow varied according to the base material plastic properties. In fact, meanwhile for the reference (AA6063-T6) and HSLSRS

materials, it was previewed that the material is dragged from the advancing to the retreating side of the tool, being deposited approximately one pin diameter backwards, after one revolution, for the low strength materials (LSHSRS and LSLSR) and for the high strength material with high strain rate sensitivity (HSHSRS), it was previewed that the material is stirred under the shoulder for more than one revolution before being deposited in the rear of the tool.

In Figure 12 are now shown the strain rates and temperatures registered for the different materials once steady state conditions were reached during welding. The figure shows that meanwhile the temperatures reached during welding increase with the materials strength at high temperatures, the strain rates diminish, being lower for the materials with higher strain rate sensitivity. So, from the results in Figure 12, it is possible to conclude that welds with the coarser and more uniform grain structure result from the welding of high strength materials, as a result of the narrower range of strain rates experienced during welding.

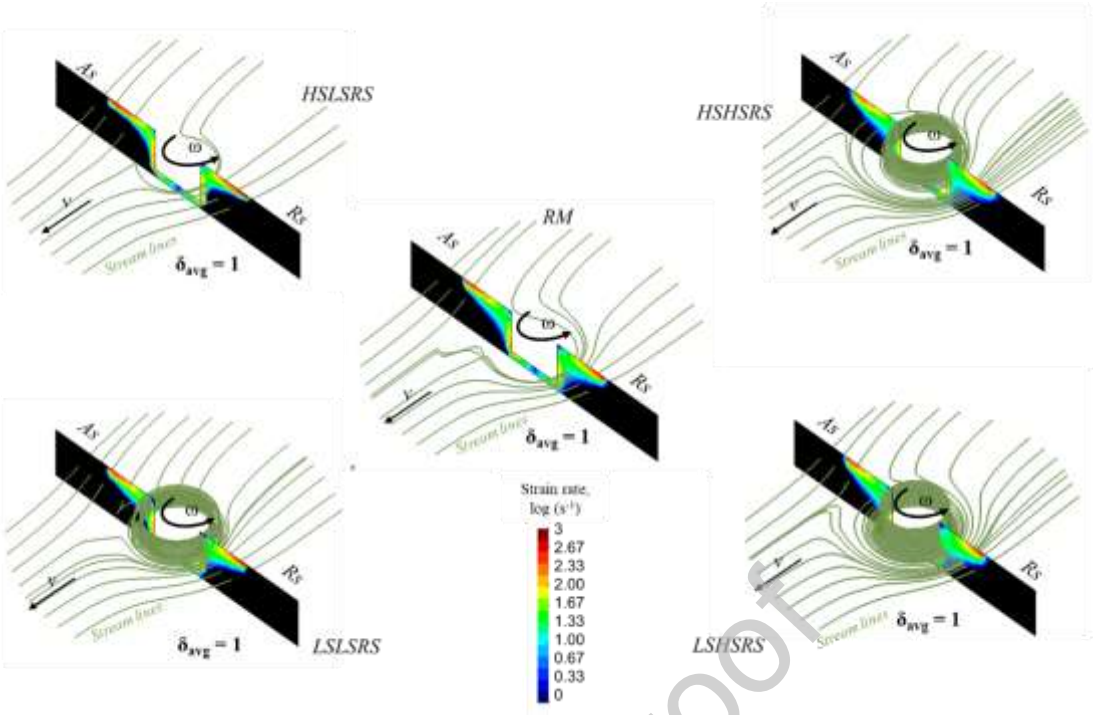


**Figure 11 –** Evolution of the welding streamlines and logarithmic equivalent strain rate with the base material plastic properties. Labels *As*, *Rs*, *δ*, *ω* and *v* denote advancing side, retreating side, sticking fraction, rotation speed and traverse speed, respectively.

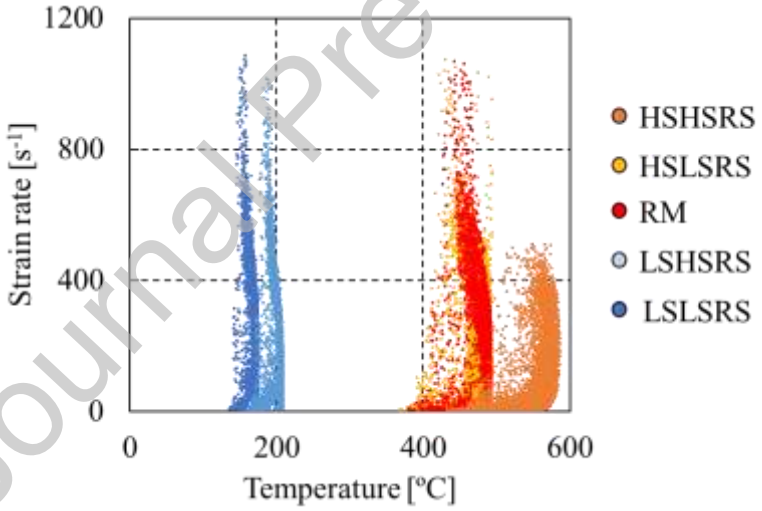


**Figure 12 –** Strain rates and temperatures registered for the different materials. Labels *HSHSRS* and *HSLSRS* denote high strength materials with high and low strain rate sensitivity, respectively. Labels *LSHSRS* and *LSLSRS* denote low strength materials with high and low strain rate sensitivity, respectively. Label *RM* denote reference material.

## 4. Conclusions

In the present work, the influence of the welding velocities, tool dimensions and base material plastic properties on the contact conditions, strain rates and temperatures in

FSW was analysed by using a coupled 3D thermo-mechanical numerical model. The following conclusions were reached:

- The numerical model is able to predict the evolution of the contact conditions with the welding time and processing parameters, as well as of capturing the non-uniform contact conditions at the tool/workpiece interface.
- The numerical model is able to predict with satisfactory accuracy the temperature and strain rate gradients in the stirred volume, enabling to calculate the grain size distribution in the stirred volume using the Zener-Hollomon parameter ($Z$). Using this parameter, it was concluded that in order to obtain a refined microstructure in the welds it is advisable the use of small diameter tools, to minimise heat generation, and high rotation speeds, to maximise the strain rate.
- The welding temperatures may be estimated using processing parameters and tool dimensions, for welding conditions corresponding to an average sticking fraction larger than 20%. The highest temperatures are reached for sticking fractions higher than 80% and/or high strength materials.
- The material flow during welding is determined by the base material plastic properties, in first, and by the contact conditions at the tool/workpiece interface, in second. Independently of the base material properties, non-defective welds may be produced when the average sticking fraction is higher than 50%.
- High strength materials with high strain rate sensitivity are more likely to display coarse grain structures than low strength materials, due to the important influence of the plastic properties on the strain rate and heat generation.



**Acknowledgements**

This research is sponsored by FEDER funds through Portugal 2020 (PT2020), by the Competitiveness and Internationalization Operational Program (COMPETE 2020) and national funds through the Portuguese Foundation for Science and Technology, under the projects: UID/EMS/00285/2020, POCI-01-0145-FEDER-00763 and Friction 4.0 (POCI-01-0145-FEDER-032089). The author, D.G. Andrade is supported by the Portuguese Foundation for Science and Technology through SFRH/BD/130196/2017 fellowship. All supports are gratefully acknowledged.

**Credit Author Statement**

**D.G Andrade:** Conceptualization, Validation, Writing - Original Draf. **C. Leitão:** conceptualization, Validation, Writing - Original Draf. **N. Dialami:** Software, Resources. **M. Chiumenti:** Software, Resources **D.M. Rodrigues:** Supervision, Conceptualization, Validation, Writing - Original Draf

**Declaration of interests**

The authors declare that they have no known competing financial interests or personal relationships that could have appeared to influence the work reported in this paper.

**Graphical abstract**

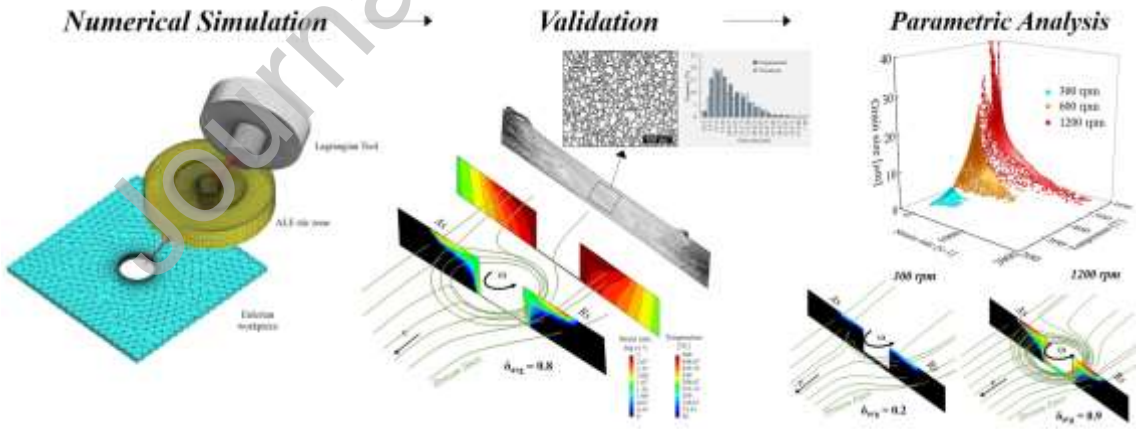


**References**

[1] Frigaard Ø, Grong Ø, Midling OT. A process model for friction stir welding of age hardening aluminum alloys. Metall Mater Trans A 2001;32:1189–200. doi:10.1007/s11661-001-0128-4.

[2] Gerlich A, Avramovic-Cingara G, North TH. Stir zone microstructure and strain rate during Al 7075-T6 friction stir spot welding. Metall Mater Trans A 2006;37:2773–86. doi:10.1007/BF02586110.

[3] Gerlich A, Su P, Yamamoto M, North TH. Effect of welding parameters on the strain rate and microstructure of friction stir spot welded 2024 aluminum alloy. J Mater Sci 2007;42:5589–601. doi:10.1007/s10853-006-1103-7.

[4] Masaki K, Sato YS, Maeda M, Kokawa H. Experimental simulation of recrystallized microstructure in friction stir welded Al alloy using a plane-strain compression test. Scr Mater 2008;58:355–60. doi:https://doi.org/10.1016/j.scriptamat.2007.09.056.

[5] Chen ZW, Cui S. Strain and strain rate during friction stir welding/processing of Al-7Si-0.3Mg alloy. {IOP} Conf Ser Mater Sci Eng 2009;4:12026. doi:10.1088/1757-899x/4/1/012026.

[6] Liu XC, Sun YF, Nagira T, Ushioda K, Fujii H. Experimental evaluation of strain and strain rate during rapid cooling friction stir welding of pure copper. Sci Technol Weld Join 2019;24:352–9. doi:10.1080/13621718.2018.1556436.

[7] Morisada Y, Imaizumi T, Fujii H. Determination of strain rate in Friction Stir Welding by three-dimensional visualization of material flow using X-ray radiography. Scr Mater 2015;106:57–60. doi:https://doi.org/10.1016/j.scriptamat.2015.05.006.

[8] Morisada Y, Imaizumi T, Fujii H. Clarification of material flow and defect formation during friction stir welding. Sci Technol Weld Join 2015;20:130–7. doi:10.1179/1362171814Y.0000000266.

[9] Kumar R, Pancholi V, Bharti RP. Material flow visualization and determination of strain rate during friction stir welding. J Mater Process Technol 2018;255:470–6. doi:https://doi.org/10.1016/j.jmatprotec.2017.12.034.

[10] Chang CI, Lee CJ, Huang JC. Relationship between grain size and Zener–Holloman parameter during friction stir processing in AZ31 Mg alloys. Scr Mater 2004;51:509–14. doi:https://doi.org/10.1016/j.scriptamat.2004.05.043.

[11] Long T, Tang W, Reynolds AP. Process response parameter relationships in

aluminium alloy friction stir welds. Sci Technol Weld Join 2007;12:311–7. doi:10.1179/174329307X197566.

[12] Nandan R, Roy GG, Lienert TJ, DebRoy T. Numerical modelling of 3D plastic flow and heat transfer during friction stir welding of stainless steel. Sci Technol Weld Join 2006;11:526–37. doi:10.1179/174329306X107692.

[13] Nandan R, Roy GG, Debroy T. Numerical simulation of three-dimensional heat transfer and plastic flow during friction stir welding. Metall Mater Trans A 2006;37:1247–59. doi:10.1007/s11661-006-1076-9.

[14] Nandan R, Roy GG, Lienert TJ, Debroy T. Three-dimensional heat and material flow during friction stir welding of mild steel. Acta Mater 2007;55:883–95. doi:https://doi.org/10.1016/j.actamat.2006.09.009.

[15] Du Y, Mukherjee T, Mitra P, DebRoy T. Machine learning based hierarchy of causative variables for tool failure in friction stir welding. Acta Mater 2020;192:67–77. doi:https://doi.org/10.1016/j.actamat.2020.03.047.

[16] Mukherjee S, Ghosh AK. Flow visualization and estimation of strain and strain-rate during friction stir process. Mater Sci Eng A 2010;527:5130–5. doi:https://doi.org/10.1016/j.msea.2010.04.091.

[17] Ammouri AH, Kridli G, Ayoub G, Hamade RF. Relating grain size to the Zener-Hollomon parameter for twin-roll-cast AZ31B alloy refined by friction stir processing. J Mater Process Technol 2015;222:301–6. doi:10.1016/j.jmatprotec.2015.02.037.

[18] Sharghi E, Farzadi A. Simulation of strain rate, material flow, and nugget shape during dissimilar friction stir welding of AA6061 aluminum alloy and Al-Mg2Si composite. J Alloys Compd 2018;748:953–60. doi:https://doi.org/10.1016/j.jallcom.2018.03.145.

[19] Hamilton C, Dymek S, Sommers A. A thermal model of friction stir welding in aluminum alloys. Int J Mach Tools Manuf 2008;48:1120–30. doi:https://doi.org/10.1016/j.ijmachtools.2008.02.001.

[20] Li W, Zhang Z, Li J, Chao YJ. Numerical Analysis of Joint Temperature Evolution During Friction Stir Welding Based on Sticking Contact. J Mater Eng

Perform 2012;21:1849–56. doi:10.1007/s11665-011-0092-0.

[21] Yu Z, Zhang W, Choo H, Feng Z. Transient Heat and Material Flow Modeling of Friction Stir Processing of Magnesium Alloy using Threaded Tool. Metall Mater Trans A 2012;43:724–37. doi:10.1007/s11661-011-0862-1.

[22] Colegrove PA, Shercliff HR. 3-Dimensional CFD modelling of flow round a threaded friction stir welding tool profile. J Mater Process Technol 2005;169:320–7. doi:https://doi.org/10.1016/j.jmatprotec.2005.03.015.

[23] Chen GQ, Shi QY, Li YJ, Sun YJ, Dai QL, Jia JY, et al. Computational fluid dynamics studies on heat generation during friction stir welding of aluminum alloy. Comput Mater Sci 2013;79:540–6. doi:10.1016/j.commatsci.2013.07.004.

[24] Chen G, Feng Z, Zhu Y, Shi Q. An Alternative Frictional Boundary Condition for Computational Fluid Dynamics Simulation of Friction Stir Welding. J Mater Eng Perform 2016;25:4016–23. doi:10.1007/s11665-016-2219-9.

[25] Robe H, Claudin C, Bergheau J-M, Feulvarch E. R-ALE simulation of heat transfer during friction stir welding of an AA2xxx/AA7xxx joint on a large process window. Int J Mech Sci 2019;155:31–40. doi:https://doi.org/10.1016/j.ijmecsci.2019.02.029.

[26] Ghate ND, Sood A, Srivastava A, Shrivastava A. Ductile fracture based joint formation mechanism during friction stir welding. Int J Mech Sci 2020;168:105293. doi:https://doi.org/10.1016/j.ijmecsci.2019.105293.

[27] Iqbal MP, Tripathi A, Jain R, Mahto RP, Pal SK, Mandal P. Numerical modelling of microstructure in friction stir welding of aluminium alloys. Int J Mech Sci 2020;185. doi:10.1016/j.ijmecsci.2020.105882.

[28] Colligan KJ, Mishra RS. A conceptual model for the process variables related to heat generation in friction stir welding of aluminum. Scr Mater 2008;58:327–31. doi:https://doi.org/10.1016/j.scriptamat.2007.10.015.

[29] Hamilton C, Sommers A, Dymek S. A thermal model of friction stir welding applied to Sc-modified Al–Zn–Mg–Cu alloy extrusions. Int J Mach Tools Manuf 2009;49:230–8. doi:https://doi.org/10.1016/j.ijmachtools.2008.11.004.

[30] Roth A, Hake T, Zaeh MF. An Analytical Approach of Modelling Friction Stir

Welding. Procedia CIRP 2014;18:197–202. doi:https://doi.org/10.1016/j.procir.2014.06.131.

[31] Wang H, Colegrove PA, dos Santos JF. Numerical investigation of the tool contact condition during friction stir welding of aerospace aluminium alloy. Comput Mater Sci 2013;71:101–8. doi:https://doi.org/10.1016/j.commatsci.2013.01.021.

[32] Chen G, Ma Q, Zhang S, Wu J, Zhang G, Shi Q. Computational fluid dynamics simulation of friction stir welding: A comparative study on different frictional boundary conditions. J Mater Sci Technol 2018;34:128–34. doi:https://doi.org/10.1016/j.jmst.2017.10.015.

[33] Meyghani B, Wu C. Progress in Thermomechanical Analysis of Friction Stir Welding. Chinese J Mech Eng 2020;33:12. doi:10.1186/s10033-020-0434-7.

[34] Chiumenti M, Cervera M, Agelet de Saracibar C, Dialami N. Numerical modeling of friction stir welding processes. Comput Methods Appl Mech Eng 2013;254:353–69. doi:https://doi.org/10.1016/j.cma.2012.09.013.

[35] Dialami N, Chiumenti M, Cervera M, Agelet de Saracibar C. An apropos kinematic framework for the numerical modeling of friction stir welding. Comput Struct 2013;117:48–57. doi:https://doi.org/10.1016/j.compstruc.2012.12.006.

[36] Dialami N, Cervera M, Chiumenti M, Agelet de Saracibar C. A fast and accurate two-stage strategy to evaluate the effect of the pin tool profile on metal flow, torque and forces in friction stir welding. Int J Mech Sci 2017;122:215–27. doi:https://doi.org/10.1016/j.ijmecsci.2016.12.016.

[37] Dialami N, Chiumenti M, Cervera M, Segatori A, Osikowicz W. Enhanced friction model for Friction Stir Welding (FSW) analysis: Simulation and experimental validation. Int J Mech Sci 2017;133:555–67. doi:https://doi.org/10.1016/j.ijmecsci.2017.09.022.

[38] Dialami N, Chiumenti M, Cervera M, de Saracibar C, Ponthot JP. Material flow visualization in Friction Stir Welding via particle tracing. Int J Mater Form 2015;8:167–81. doi:10.1007/s12289-013-1157-4.

[39] Dialami N, Cervera M, Chiumenti M, Segatori A. Prediction of joint line remnant

defect in friction stir welding. Int J Mech Sci 2019;151:61–9. doi:https://doi.org/10.1016/j.ijmecsci.2018.11.012.

[40] Andrade DG, Leitão C, Dialami N, Chiumenti M, Rodrigues DM. Modelling torque and temperature in Friction Stir Welding of Aluminium Alloys. Int J Mech Sci 2020:105725. doi:https://doi.org/10.1016/j.ijmecsci.2020.105725.

[41] Zhang YN, Cao X, Larose S, Wanjara P. Review of tools for friction stir welding and processing. Can Metall Q 2012;51:250–61. doi:10.1179/1879139512Y.0000000015.

[42] Prado RA, Murr LE, Shindo DJ, Soto KF. Tool wear in the friction-stir welding of aluminum alloy 6061+20 Al 2 O 3 : a preliminary study. Scr Mater 2001;45:75–80.

[43] Schmidt H, Hattel J, Wert J. An analytical model for the heat generation in friction stir welding. Model Simul Mater Sci Eng 2003;12:143–57. doi:10.1088/0965-0393/12/1/013.

[44] Leal RM, Leitão C, Loureiro A, Rodrigues DM, Vilaça P. Material flow in heterogeneous friction stir welding of thin aluminium sheets: Effect of shoulder geometry. Mater Sci Eng A 2008;498:384–91. doi:https://doi.org/10.1016/j.msea.2008.08.018.

[45] Arbegast WJ. A flow-partitioned deformation zone model for defect formation during friction stir welding. Scr Mater 2008;58:372–6. doi:https://doi.org/10.1016/j.scriptamat.2007.10.031.

[46] Dialami N, Chiumenti M, Cervera M, Agelet de Saracibar C, Ponthot JP, Bussetta P. Numerical Simulation and Visualization of Material Flow in Friction Stir Welding via Particle Tracing BT - Numerical Simulations of Coupled Problems in Engineering. In: Idelsohn SR, editor., Cham: Springer International Publishing; 2014, p. 157–69. doi:10.1007/978-3-319-06136-8_7.

[47] Huang K, Logé RE. A review of dynamic recrystallization phenomena in metallic materials. Mater Des 2016;111:548–74. doi:https://doi.org/10.1016/j.matdes.2016.09.012.

[48] Zhao Y-H, Lin S-B, He Z-Q, Wu L. Microhardness prediction in friction stir

welding of 2014 aluminium alloy. Sci Technol Weld Join 2006;11:178–82. doi:10.1179/174329306X84391.

[49] Sheppard T, Jackson A. Constitutive equations for use in prediction of flow stress during extrusion of aluminium alloys. Mater Sci Technol 1997;13:203–9. doi:10.1179/mst.1997.13.3.203.

[50] Fonda RW, Knipling KE. Texture development in friction stir welds. Sci Technol Weld Join 2011;16:288–94. doi:10.1179/1362171811Y.0000000010.

[51] Balachandran S, Mishra RS, Banerjee D. Friction stir processing of a metastable β titanium alloy in β and α+β phase fields. Mater Sci Eng A 2020;772:138705. doi:https://doi.org/10.1016/j.msea.2019.138705.

[52] Jia B, Rusinek A, Pesci R, Bahi S, Bernier R. Thermo-viscoplastic behavior of 304 austenitic stainless steel at various strain rates and temperatures: Testing, modeling and validation. Int J Mech Sci 2020;170:105356. doi:https://doi.org/10.1016/j.ijmecsci.2019.105356.